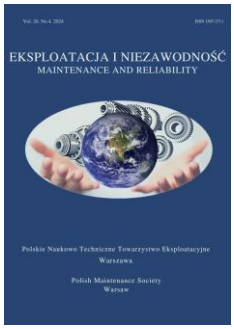

Eksploatacja i Niezawodnosc – Maintenance and Reliability

Volume 26 (2024), Issue 4

journal homepage: http://www.ein.org.pl

Article citation info:
Zhou J, Liu L, Li J, Multi-objective optimization design of rail grinding profile in Curve Section of Subway based on wear Evolution and representative worn profile, Eksploatacja i Niezawodnosc – Maintenance and Reliability 2024: 26(4) http://doi.org/10.17531/ein/191472

Multi-objective optimization design of rail grinding profile in Curve Section of Subway based on wear Evolution and representative worn profile

Indexed by:

Jun Zhou[a,b,*], Linya Liu[a,c], Jiyang Li[a,]

[a] East China Jiaotong University, China
[b] Jiangxi Industrial Polytechnic College, China
[c] Pingxiang University, China

Highlights

- This study utilizes Dynamic Time Warping (DTW) to select a representative rail worn profile for optimization design from the rail worn profile.
- This paper proposes an optimization mathematical model that considers the evolution of wheel profile wear for design optimization.
- Adaptive weight adjustment factor coefficients are introduced to avoid the subjective influence of the designer's experience.

Abstract

The grinding of curved rails is a crucial aspect of subway maintenance and repair. It effectively reduces wear. This paper proposes a multi-objective optimization design method for grinding profiles in curved sections. First, the Dynamic Time Regularisation (DTW) algorithm selects representative grinding profiles as the initial population. Then, the optimal design region is determined through wear characterization analysis. Mathematical expressions of wheel profiles are selected as design variables to build a parametric model. Next, the predictive model that considers the evolution of wheel wear is incorporated into the multi-objective function. The objective function's adaptive weight adjustment coefficient factors are introduced to establish the multi-objective optimization model for wheel profiles. The Latin hypercubic sampling method establishes the RBF agent model for simulation calculation. The optimization design of wheel profiles is carried out using the TS-NSGA-II multi-objective algorithm. Finally, a comparative verification analysis is conducted to assess the profiles before and after optimization. This analysis includes three key aspects: wheel wear evolution analysis, wheel-rail static contact analysis, and vehicle dynamics performance analysis.

Keywords
wheel-rail wear, dynamic time warping, TS-NSGA-II algorithm, representative worn rail profiles, and rail grinding removal amount.

1. Introduction

Steel rails are a crucial rail system component, supporting vehicles and playing vital roles in vehicle guidance, force transmission for driving and braking, and forming rail circuits. However, the repeated rolling contact between rails and wheels on their contact surfaces can lead to problems caused by fatigue and wear. These problems include localized collapse of rail surfaces, block stripping, and multiple cracking disorders. Such issues shorten the rail's lifespan and can result in serious accidents. Particularly in curved tracks, the contact stress between the wheel flange and rail surface is higher than in straight tracks. This will lead to increased wear on both the wheel and rail, shorter grinding and replacement cycles for the rail, increased noise, and a decline in ride comfort. Traditional wheel and rail profile designs mainly focus on the wheel and rail profile design. These designs heavily rely on the designer's experience. However, with the rapid advancement of computing

(*) Corresponding autho
E-mail addresses: J. Zhou (ORCID: 0009-0003-0079-586X) zhoujunjxnc@163.com, L. Liu, lly1949@163.com, J. Li, 793678981@qq.com

technology, numerical design methods involving numerical simulation and optimization techniques are widely utilized for optimizing wheel-rail profiles.

In recent years, domestic and international scholars have made significant progress in wheel-rail matching and profile optimization design. They have proposed numerous new methods for deriving optimal wheel-rail profiles, which aim to enhance railroad systems' performance, safety, and efficiency.

For instance, Lin et al.1developed and established a numerical calculation method for the rail grinding mode in the GMC96 rail grinding train. This method considers the rail's grinding target profile and each grinding stone's grinding capacity. It includes calculations for the appropriate grinding angle and grinding power for each grinding stone. Li et al. 2focused on accurately predicting rail wear to optimize wheel-rail profiles and the rail grinding cycle. This was achieved by introducing a numerical model predicting rail wear as the total passing weight increases. Wang et al.3presented a rail profile optimization method that considers the wear rate over the design cycle. The objective is to minimize rail wear in curves on large freight tracks and extend the life of the rails. In order to facilitate the modification of the target profile, Zeng et al.4 utilized non-uniform rational B-spline curves in the asymmetric grinding region to establish a parametric model of the rail head curve. Liang et al.5proposed an algorithm to estimate the rail profile using the vehicle's vertical acceleration resulting from train-rail dynamics interaction. Based on actual speed and energy data collected from a real urban rail system, Huang et al.6proposed a data-driven model and a comprehensive heuristic algorithm based on machine learning. This model aims to determine the optimal speed profile with minimum energy consumption. Ye et al.7proposed a method that combines the regression capability of the Kriging Surrogate Model (KSM) with the iterative computational power of particle swarm optimization (PSO). This approach allows for quick and reliable profile optimization. In order to reduce rail wear and achieve sustainable transportation, Jiang et al.8proposed an approach that combines artificial neural networks (ANN) and genetic algorithms (GA) for track contour optimization. Pacheco et al.9 introduced a methodology for developing optimal railway wheel profiles by considering their rolling contact fatigue (RCF) and wear performance. Qi et al.10 introduced a novel Gaussian Function Correction (GFC) method for designing a new rail profile. This method incorporates two parameters to control the wear region. The Kriging Surrogate Model (KSM) is used to reduce the number of simulations, and the Non-dominated Sorting Genetic Algorithm-II (NSGA-II) is employed to optimize the rail profile. Lin et al.11 developed a rail profile curve reconstruction method based on the theory of NURBS curves. Additionally, they proposed an economical grinding design method for rail profiles in freight railroads based on the Archard wear computation model. Shi et al.12 introduced a technique whereby two fixed and multiple movable points were strategically positioned on the rail profile. The NURBS method was then utilized to generate a novel profile. Zhai et al.13developed an asymmetric design for the inner and outer rail profiles of the 600 m curve on the China Shuohuang heavy load line. Subsequently, the operational performance of the rail profile was tested, resulting in a reduction of 30%-40% in wear on the curve side. Mao et al. 14introduced an inverse design approach that utilizes the ideal rolling radii difference (RRD) function to optimize rail grinding profiles.

This study utilizes the dynamic time regularization (DTW) algorithm to select representative profiles from rail wear profiles for design optimization to optimize rail grinding target profiles. Traditional methods often only focus on the initial profile and overlook the evolution of wheel profiles due to wear[15-23]. An optimization mathematical model considering the evolution of wheel profile wear is employed to address this limitation, along with introducing adaptive weight adjustment factors to mitigate the subjective influence of the multi-objective function weights.

Currently, most multi-objective optimization algorithms are based on genetic algorithms (GA), with the non-dominated sorting genetic algorithm II (NSGA-II) being a commonly used method. However, traditional NSGA-II requires significant computational resources when tackling complex combinatorial optimization problems, especially with large search spaces. In order to enhance solution efficiency and accuracy, this study adopts the hybrid TS-NSGAII algorithm, which combines the strengths of different algorithms. This approach allows for more efficient problem space exploration, population diversity maintenance, local optima avoidance, and improved

approximation of the Pareto frontier.

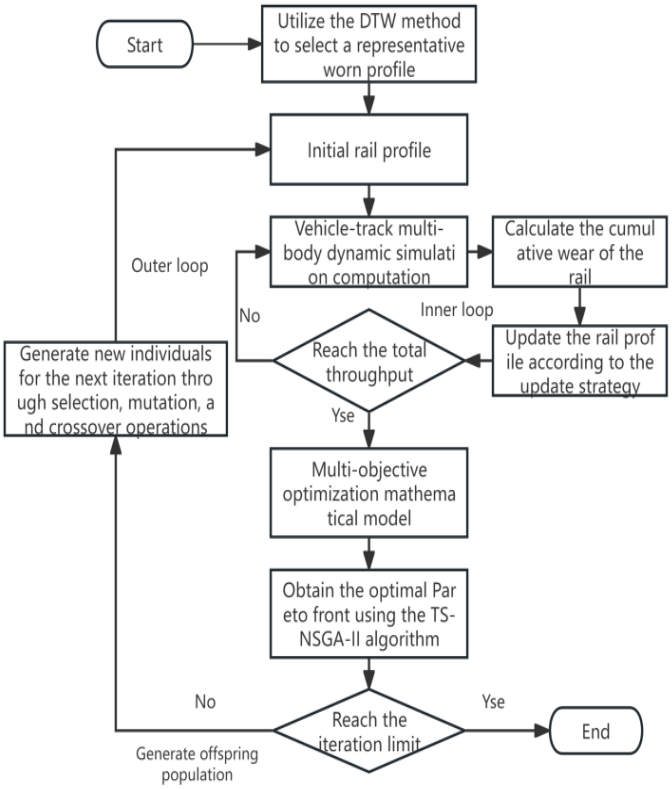

Fig.1. Flowchart of the wheel profile optimization process.

2. Multi-objective optimization design method of wheel profile

2.1. Profile Optimization Procedure

The multi-objective optimization design method for rail profiles comprises six main modules, as illustrated in Fig.

(1) Wear characteristics analysis and representative profile selection module: This module involves tracking measurements of rail profile wear in the test section, analyzing the wear range and characteristics of the profile, and utilizing the dynamic time adjustment algorithm to select the representative worn profile as the initial population from the measured rail wear profile.

(2) Profile generation module: This module determines the optimization design range based on the wear characteristics analysis, selects the mathematical expression form of the wheel profile as the design variable, and determines the value range of each design variable. Using MATLAB software, the design variables are used as inputs, and the discrete points of wheel profiles are generated as outputs to create new wheel profiles.

(3) Dynamics simulation module: This module utilizes SIMPACK software to establish a vehicle dynamics model, which calculates the samples' objective function values and constraint function values. The accuracy of the model is verified based on the measured data. An agent model is also established using the radial basis function (RBF) as an approximate mathematical model. This model utilizes the sample parameters, objective function, and constraint function values to conduct fast and efficient dynamics simulations.

(4) Rail Profile Update Module: In this module, the results of the kinetic simulation are used to evaluate the incremental wear depth within the wheel-rail contact zone. The wear depth is then mapped onto the profile to update the rail profile.

(5) Multi-objective Optimization Module: This module selects the predicted wheel wear, grinding removal amount, and the axle transverse force as the optimization objective functions. It also incorporates the tipping coefficient, derailment coefficient, and curve tread geometric constraints as the constraint functions. This module establishes a multi-objective optimization approach that considers the evolution of wheel profile wear.

(6) Solver module: The TS-NSGA-II algorithm is utilized in this module to solve the multi-objective optimization problem. New populations are generated for the next iteration through global+local search, selection, mutation, and crossover operations. Modules (2) to (6) are repeated until the iteration-stopping conditions are met, resulting in the Optimal optimized profiles.

2.2. Analysis of rail wear characteristics and extraction of representative worn profiles

2.2.1. Measurement of rail wear profiles

For the Metro Line 1 system in Nanchang, China, a section of heavily worn curved tracks was selected for detailed field rail measurements. This curved section is located in a vital part of the metro network, approximately 1 km from the city center interchange station. The interchange station is a key node connecting various areas and belongs to a high-traffic zone. Consequently, this area experiences frequent train movements, necessitating regular maintenance and inspections to ensure smooth train operation and passenger safety. We utilized the Rail Profile Gauge for continuous and digital measurements to obtain crucial data regarding the rail wear profile. We carefully chose several measurement points within this specific curved area, considering the curve's radius, height, and angle. Nine

measurement points were established to cover the entire curve section and obtain detailed data about rail wear profiles. There were 36 measurements for each rail, resulting in a comprehensive analysis.

During the rail measurements, data regarding side wear, gauge angle wear, and vertical wear of the rail were acquired (refer to Fig. 2). Since this was a curved section, particular attention was given to side wear and gauge angle wear, which typically occur as trains navigate curves (refer to Table 1).

By analyzing the measured wear data of the low and high rails, it can be learned from Fig.3 that the maximum depth of vertical wear of both the low and high rails is less than 2.0mm. The low rail primarily experiences top wear within the range of [-25, 30 mm], with wear values ranging from 0.64 mm to 1.07 mm. On the other hand, the wear range of the high rail is mainly distributed within the interval of [-1,34mm]. Compared to the low rail, the high rail exhibits more severe lateral and gauge angle wear, with maximum wear depths reaching 4.915 mm and 4.144 mm, respectively. This can be attributed to the greater wheel-rail lateral force exerted on the high rail in the small radius curve section, making it more susceptible to wear and fatigue. Conversely, the low rail experiences less wheel-rail lateral force, resulting in relatively lower levels of wear and deformation.

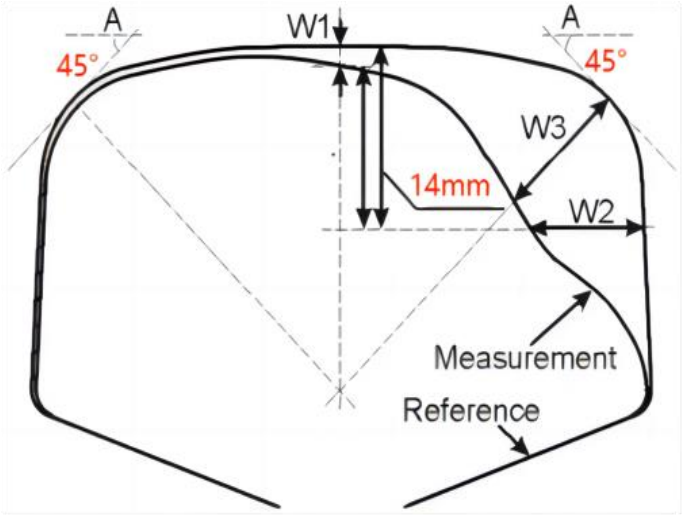

Fig.2. Schematic of rail wear measurement.

Table1 Partial low and high rail wear data

Position	Low rail wear（mm）			High rail wear（mm）		
Point	W1	W2	W3	W1	W2	W3
1	0.124	0.951	0.863	0.215	3.592	3.456
2	0.067	0.794	0.592	0.075	2.284	2.614
3	0.227	1.053	0.777	0.006	2.290	2.796
4	0.042	0.810	0.811	0.061	2.025	2.736
5	0.179	0.888	1.126	0.125	2.410	3.571
6	0.161	0.928	1.155	0.161	2.159	2.630
7	0.126	0.935	0.740	0.214	2.170	3.498
8	0.099	0.874	0.708	0.043	2.526	3.602
9	0.143	0.905	0.859	0.172	5.062	4.061

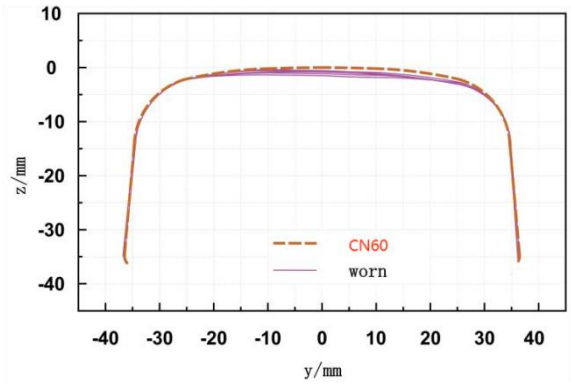

b） Low rail

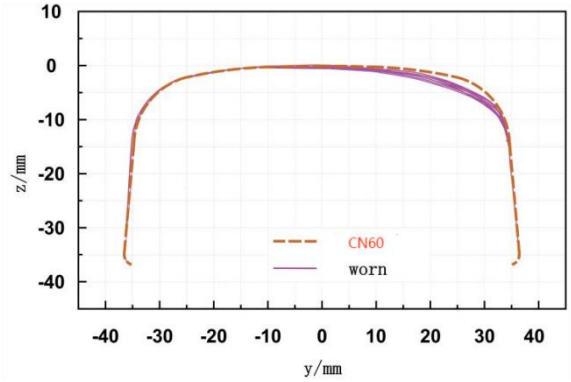

b） High rail

Fig.3. Measured worn rail profile for the curve segment.

2.2.2. Representative Profile Selection based on Dynamic Time Warping (DTW) Algorithm

The Dynamic Time Warping (DTW) algorithm is used to assess the similarity between two-time series and is particularly effective for analyzing irregularly aligned time series data24. A non-linear mapping can be applied to capture their similarity when comparing two-time series, X and Y. Fig.4 illustrates an example of such a mapping.

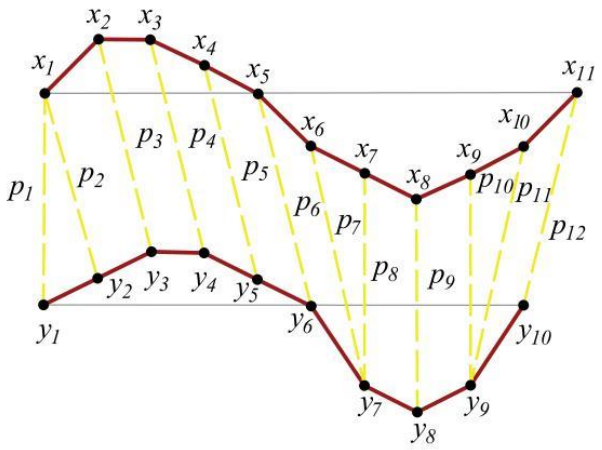

Fig.4. Alignment between two sequences X and Y.

In this study, a significant amount of rail profile data will be collected from various cross-section locations and used as input data. The Dynamic Time Warping (DTW) algorithm will calculate the DTW distance between different profiles. This distance calculation allows for identifying the most similar profile to serve as a representative example. The following steps and associated formulas outline the methodology:

Step 1: Data formatting and standardization

Firstly, the collected data should be organized into a uniform format. Each profile should be represented by an equal number of data points, denoted as N, to facilitate subsequent calculations. Data formatting can be accomplished using data processing tools or scripts. Additionally, it is important to standardize the data to ensure that the scale or units do not affect the DTW distance calculations. Standardization may involve translating, scaling, or rotating the data to establish a consistent reference point or coordinate system.

The wear profile data comprises m profiles, each consisting of n 2D XY axis data points that form a time series.

$$\begin{aligned} X_1 &= \{(x_{11}, y_{11}), (x_{12}, y_{12}), \dots, (x_{1n}, y_{1n})\} \\ X_2 &= \{(x_{21}, y_{21}), (x_{22}, y_{22}), \dots, (x_{2n}, y_{2n})\} \\ &\vdots \\ X_m &= \{(x_{m1}, y_{m1}), (x_{m2}, y_{m2}), \dots, (x_{mn}, y_{mn})\} \end{aligned} \quad (1)$$

Step 2: Dynamic Planning Calculation

The Dynamic Time Warping (DTW) algorithm is utilized to compute the DTW distances between each pair of profiles, enabling the identification of the most similar profiles for subsequent selection as representative examples.

(1) Initializing the Local Distance Matrix:

A Local Distance Matrix (LDM) of size n×n is initialized to store the local distances between two profiles, where n represents the length of the time series.

Using the chosen Euclidean distance metric, the distance between each profile i and profile j data point is calculated, populating the local distance matrix. The formula for calculating the local distance matrix (denoted as d) is as follows:

$$LDM_{i,j}(k,l) = d((x_{1k}, y_{1k}), (x_{2k}, y_{2k})) \quad (2)$$

Where $LDM_{i,j}(k,l)$ represents the elements of the local distance matrix, indicating the distance or similarity measure between the *kth* data point of profile *i* and the lth data point of profile *j*. The Accumulated Distance Matrix (ADM) is then generated to compute the accumulated distance. Initialization of the Accumulated Distance Matrix:

An n×n ADM is created, with the first row and column initialized to initial distance values. These initial distances represent the cumulative distances from the starting point to each data point. The formula for initializing the cumulative distance matrix (denoted as D) is as follows:

$$\begin{aligned} ADM_{i,j}(0,0) = LDM_{i,j}(0,0) ADM_{i,j}(k,0) = \\ LDM_{i,j}(k,0) + ADM_{i,j}(k- \\ 1,0), for k = 1,2,\dots,n-1 \quad ADM_{i,j}(0,l) = LDM_{i,j}(0,l) + \\ ADM_{i,j}(0,l-1), for k = 1,2,\dots,n-1 \end{aligned} \quad (3)$$

These initialization values represent the cumulative distance from the starting point to each data point.

(2)The cumulative distance is calculated using dynamic programming:

Beginning with $ADM_{i,j(1,1)}$, the remaining elements of the cumulative distance matrix are computed using the following update formula:

$$\begin{aligned} ADM_{i,j}(k,l) = LDM_{i,j}(k,l) + \\ min\begin{Bmatrix} ADM_{i,j}(k-1,l), ADM_{i,j}(k,l-1), \\ ADM_{i,j}(k-1,l-1) \end{Bmatrix} \end{aligned} \quad (4)$$

The main function in the equation selects the smallest value among the three neighbouring elements: one above, one to the left, and one diagonally above to the left. This minimum value is then added to the corresponding element in the current local distance matrix.

(3) Calculate DTW distance:

The DTW distance is determined by the lower right element of the cumulative distance matrix, which quantifies the DTW distance between profile *i* and profile *j*. The calculation of the DTW distance is as follows:

$$DTM_{i,j} = ADM_{i,j}(n-1, n-1) \quad (5)$$

The dynamic programming process involves the calculation of the DTW distance between two-time series using a local distance matrix and a cumulative distance matrix. Dynamic programming enables the capture of similarity between different time series, with smaller DTW distances indicating greater similarity.

Based on the calculated DTW distances, an m×m distance matrix is constructed, where the elements in the *ith* row and *jth* column represent the DTW distance between the *ith* type profile and the *jth* type profile.

Step 3: Selection of representative typefaces

In Step 2, we computed the DTW distances between each facet and all other facets. Step 3 selects the facet with the smallest average DTW distance as the representative facet. This facet exhibits the highest overall similarity to the other facets. The average DTW distance is calculated using the following formula:

$$AverageDTM_i = \frac{\sum_{i \neq j} DTM_{i,j}}{m-1} \quad (6)$$

$AverageDTW_i$ represents the average *DTW* distance of profile *i*, and $DTW_{i\,j}$ represents the DTW distance between profile *i* and profile *j*. By selecting the profile with the smallest average DTW distance, we can capture the rail wear characteristics that best represent the entire group of profiles. The samples $X = (x_1, x_2, x_3, x_4)$ with the smallest average DTW distances, ranked 1-4, are chosen as representative typical wear profiles for the initial population in the optimization design.

2.3. Mathematical modeling of rail profiles

Typical rail profiles, both domestically and internationally, are typically composed of arcs and straight lines. The wheel-rail contact area is primarily concentrated in the rail head region. Therefore, optimizing the design of the arc segments within the high rail head becomes crucial. Initially, the rail's optimization region is determined based on the wheel-rail contact area. The boundary points p_1 (x_{p1}, y_{p1}) and p_5 (x_{p5}, y_{p5}) are fixed, with their respective tangent slopes kp1 and k_{p5}.

To optimize the contour curve within the region, a 4-segment continuous tangent arc approach is employed, denoted as arcs 1 to 4. The coordinates of the center of each arc are O_1 (x_{O1}, y_{O1}) to O_4 (x_{O4}, y_{O4}), and the radii of the arcs are R_1 to R_4. Additionally, the points of tangency for the four arcs are p_2 (x_{p2}, y_{p2}) to p_4 (x_{p4}, y_{p4}). The geometric relationship of each parameter in the contour can be deduced using analytic geometry formulas.

By employing these mathematical formulas, optimizing the rail profile's contour can be accurately determined, allowing for improved design and performance of railway tracks.

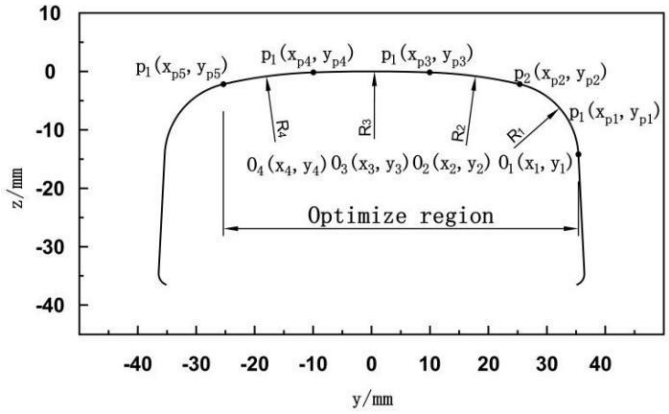

Fig.5. The geometric expression of the rail profile.

1）Calculation of the center coordinates of circle arc 1:

To determine the center coordinates of circle arc 1, we can calculate them using the known point p_1 and the given radius R_1. First, we need to calculate the angle a between the tangent line at p1 and the horizontal line. Then, we can use this angle to calculate the center circle's center coordinates.

$$\alpha = arctan(|k_{p1}|) \quad (7)$$

Since arc 1 is tangent to the fixed point p_1, the center coordinates of the circle O_1 can be determined as follows:

$$\begin{cases} x_{01} = x_{p1} - R_1 \, sin(\alpha) \\ y_{01} = y_{p1} - R_1 \, sin(\alpha) \end{cases} \quad (8)$$

2）Calculation of the vertical coordinates of the tangent point of arc 2:

The longitudinal coordinate y_{p2} of the tangent point of arc two can be calculated using the coordinates and radius of the center of arc 1, along with the transverse coordinates x_{p2} of the adjacent arc 2.

$$y_{p_2} = y_{o_1} + \sqrt{R_1^2 - \left(x_{p_2} - x_{o_1}\right)^2} \quad (9)$$

3）Calculation of the center coordinates of circle arc 2:

The center coordinates of circle arc 2, denoted as O_2, can be computed using the slope k_{12} and intercept b_{12} of the line connecting the tangent point p_2 to the center of circle O_1, along with the known longitudinal coordinates of the tangent point p_2.

$$k_{12} = (y_{p2} - y_{o1})/(x_{p2} - x_{o1})$$
$$b_{12} = -k_{12}x_{o1} + y_{o1} \quad (10)$$
$$y_{o2} = k_{12}x_{o2} + b_{12}$$

4）Determination of parameters associated with Arc Three and Arc 4:

Following a similar approach, we can calculate the longitudinal coordinates y_{p3} and y_{p4} of the tangent points of arc three and arc four and the coordinates of the centers of the circles O_3 and O_4.

5）Determination of the longitudinal coordinates of the fixed point p_5:

Finally, we must ensure that the fixed point p_5 lies on Arc 4. By calculating the ordinate y_{O4} of the center O_4 and the radius R_4 of Arc 4, we can determine the ordinate of p_5.

$$k_{34} = (y_{p_4} - y_{o_3})/(x_{p_4} - x_{o_3})\, b_{34} = -k_{34}x_{o_3} + y_{o_3}y_{o_4} =$$
$$k_{34}x_{o4} + b_{34}R_4 = \sqrt{(x_{p_5} - x_{o_4})^2 + (y_{p_5} - y_{o_4})^2} \quad (11)$$

In this manner, we obtain the design variables and related formulas for the contour curve of the rail within the optimized region. The contour curve within the optimized region can be described by the following parameters: the radii of the arcs (R_1, R2, R_3), representing the radii of the four consecutive tangent segments of the arc, and the horizontal coordinates of the tangent points (x_{p2}, x_{p3}, x_{p4}), indicating the positions of the tangent points in the horizontal direction. Therefore, the design variables can be defined as d_s=(R_1, R_2, R_3, x_{p2}, x_{p3}, x_{p4}). Adjusting these variables can optimize the track design to meet specific engineering requirements or performance specifications.

The 4-segment tangent arc G_i can be expressed as:

$$G_i = g_i(d_s) \quad (12)$$

Where $g_i(d_s)$ (i = 1, 2, 3, 4) represents the analytical equation of the circular arc segment i.

The rail profile curve G_r within the optimized region can be expressed as:

$$G_r = g_r(d_s) \quad (13)$$

Where $g_r(d_s)$ represents the analytical equation of the circular arc within the optimized region.

Since the rail with a small radius curve adopts asymmetric grinding, the grinding parameters of the high and low rails are not the same. Therefore, the design variables of the high and low rails need to be optimized separately. The model variables can be expressed as:

Since the small radius curve rail adopts asymmetric grinding, the grinding parameters for the high and low rails are not the same. Therefore, the design variables for the high and low rails need to be optimized separately. Thus, the model variables can be expressed as follows:

$$d = (d_{sh}, d_{sl}) \quad (14)$$

Where d_{sh} and d_{sl} are the design variables for the high and low rails, respectively.

2.4. Optimize the mathematical model

The wheel profile optimization problem can be described as optimizing the design variables **d**=(R_1, R_2, R_3, x_{p2}, x_{p3}, x_{p4}). The optimization model can be expressed as follows:

$$\begin{cases} Minimize: J_i(\mathbf{d}) \quad i = 1 \cdots 2 \\ \text{Subject to}: G_j(\mathbf{d}) \le G_0(\mathbf{d}) \quad j = 1 \cdots 3 \\ \mathbf{d}_W \le \mathbf{d} \le \mathbf{d}_L \end{cases} \quad (15)$$

J_i(**d**) represents the objective function, and G_i(**d**) satisfies the inequality constraints of the safety criterion. The upper and lower bounds of the design variables are $\mathbf{d}_w$ and $\mathbf{d}_L$, respectively.

2.4.1. Objective function

(1) Cumulative wear amount

The prediction of rail profile wear is conducted using the wear index-based wear model proposed by BRAGHIN 25. To determine the wear coefficients in the rail wear modeling process, we refer to the *Tγ/A* wear rate function of our CL60 wheel material matched with U71Mn rail material26. The analytical expression of the wear rate function is as follows:

$$K_B = \begin{cases} 3.58I_w & I_w < 5 \\ 17.9 & 5 \le I_w \le 20 \\ 12.3I_w - 228 & I_w > 20 \end{cases} \quad (16)$$

Where K_B/[μg/(m·mm^2)] is the wear rate of the material when rolling unit distance per unit contact area; I_w/(N/mm^2) is the friction work in the unit cell area within the contact patch; I_w can be estimated by the wear index:

$$I_w(x_i, y_j) = T_{ij}\gamma_{ij}/A_{ij} = p(x_i, y_j) \cdot \gamma(x_i, y_j) \quad (17)$$

Where $P(x_i,y_j)$ represents the magnitude of tangential stress and $\gamma(x_i,y_j)$ denotes the creep-slip displacement within each cell (x_i,y_j) in the contact patch.

The contact area is discretized, as shown in Fig. 6, to evaluate the loss of wheel material. The incremental wear depth is then calculated individually for each cell (x_i,y_j) within a given

time step t, as shown in Eq. 18.

$$\Delta Z_w(x_i, y_j) = K_w \cdot \frac{V\Delta t}{\rho} \tag{18}$$

Where ρ、V *and* K_w represent the material density, travel speed, and wear rate functions, respectively, after determining the wear depth at each cell, the wear depth in a non-rotating planar coordinate system can be defined. Eq.19 integrates over the longitudinal axis of the contact area from $-a(y_j)$ to $a(y_j)$ and then averages the values along the wheel's circumference. This allows for the prediction of the wear of a single cross-section of the wheel at $y = y_j$ as follows:

$$\Delta \bar{Z}_w(y_j) = \frac{1}{2\pi r(y_j)} \cdot \frac{V\Delta t}{\rho} \cdot \int_{-a(y_j)}^{a(y_j)} K_w \cdot dx \tag{19}$$

According to the transverse displacement distribution of the wheel contact points during the dynamic simulation, the wear at all contact spots can be superimposed to obtain the total rail wear amount. The formula for calculating the wheel wear amount is as follows:

$$J_1(\mathbf{d}) = \omega \cdot \frac{h}{2\pi r} \cdot \int_{ts}^{te} \Delta \bar{Z}_w(y_j) \cdot \frac{V\Delta t}{\rho} \tag{20}$$

Where ω is the amplification factor,r represents the radius of the wheel rolling circle, t_s is the start time of the simulation calculation, $_{he}$ is the end time, and h represents the spacing between the sampling points. The contact spot parameter information is collected once every h sampling point during the dynamic simulation. When the wheel completes one full rotation, $2\pi R/h$ contact spots are obtained. Since the same part of the wheel only contacts once during one rotation, the calculated wheel wear is divided by $2\pi R/h$, and the wear of all contact spots obtained from one rotation is averaged into one contact spot wear.

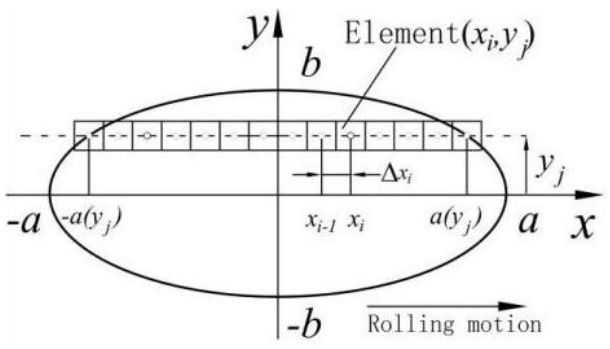

Fig. 6. Discretization of contact patch for slip evaluation.

The wear of the rail profile gradually changes with the increase in the number of train passes, known as wear evolution. Simulating this wear evolution process in numerical simulation is challenging. Based on the actual situation of the metro, the length of operation will be 17 hours per day, and the number of calculated trips will be increased during the peak period so that approximately 300 trips will be operated per day. The annual train throughput is estimated to be 90 million passes based on calculations for 8-car trains. In the simulation calculation, the updated passing amount for the rail profile is set to 75,000 passes, and the total simulated passing amount is set to 90 million passes. After each calculation of rail wear, the wear distribution is smoothed, and the profile is updated according to the updated strategy until it reaches the preset passing volume. The rail wear prediction process involves multiple profile updates to account for changes in the geometry of the rail profile, allowing for the automatic consideration of wear evolution in the optimization process.

(2) Amount of Rail Grinding Removal

$$W \left| \int_a^b g_{l-\text{wear}}(x)dx - \int_a^b g_{l-opt}(x)dx \right|_{min} + \beta \left| \int_a^b g_{h-\text{wear}}(x)dx - \int_a^b g_{h-opt}(x)dx \right| \tag{21}$$

$W_{\min}$ represents the difference between the area of the worn profile and the optimized profile, indicating the amount of rail grinding. $g_{l\text{-wear}}(x)$ and $g_{h\text{-wear}}(x)$ are the typical worn representative profile curve equations for the low and high rails. After optimization, $g_{l\text{-}opt}$ (x) and $g_{h\text{-}opt}$(x) are the low and high rail profile *curve equations. a* and *b* represent the left and right boundaries of the optimized region of the rail profile, i.e., the fixed points on the left and right sides of the optimized region. α and β are the weighting coefficients for rail grinding. Based on engineering experience in rail grinding and maintenance processes, α=0.4 and β=0.6 are used in the calculation.

(3) Wheelset lateral force

Wheelset lateral force is a crucial parameter for assessing the stability and safety of the rail system. It plays a significant role in ensuring smooth train operations and passenger safety. By employing appropriate wheel and rail profile designs, the magnitude of the wheelset lateral force can be effectively minimized, thereby enhancing the safety and reliability of the railroad system. The objective function for the wheelset lateral force is expressed as follows:

$$C_i = \max\ (|Q_{i_w} - Q_{i_n}|) \tag{22}$$

Q_{ih} and Q_{il} are the transverse forces of the high and low rails, respectively.

(4) Comprehensive Objective Function

1） Normalization of objective function values:

To enable comparison between objective function values, it is necessary to normalize each value between 0 and 1. Let $J_i(\mathbf{d})$ represent the value of the ith objective function. The normalized objective function value can be calculated as follows:

$$J_i'(d) = \frac{J_i(d) - Jd_{min}}{Jdd_{min_{max}}} \quad (23)$$

$J_{min}(\mathbf{d})$ is the minimum value of the ith objective function, and $J_{max}(\mathbf{d})$ is the maximum value.

2）Fitness Function

The fitness value of a solution is determined by calculating a weighted sum of the normalized objective function values. The fitness function can be expressed as:

$$F = \sum_{j=1}^{m} \lambda_j \cdot J_i'(d) \quad (24)$$

Where λ_j represents the weighting factor for the jth objective function.

3)Dynamic update of weight adjustment coefficients:

An adaptive weight adjustment coefficient is introduced to consider the impact of wheel profile changes on each optimization objective. The weight adjustment factor λ_j is updated based on the performance of the solutions in the population during the evolutionary process, specifically the proportion of better solutions.

Let N represent the total number of solutions and m denote the number of objective functions in the population. For the ith solution, the value of the normalization function under the jth objective function is F_{ij}. The weight adjustment factor λ_i for the jth objective function can be updated using the following equation:

$$\lambda_j = \frac{\sum_{i=1}^{N} F_{ij}}{\sum_{j=1}^{m}\sum_{i=1}^{N} F_{ij}} \quad (25)$$

Where the weight adjustment factor depends on the relative proportion of the normalization function values of each solution in the entire population, objectives with higher normalization function values will have higher proportions in the weights, making them more likely to be retained or selected in the next generation of solutions.

By employing this adaptive weight adjustment method, the algorithm can dynamically adjust the weights of the objective functions during the search process, better adapting to the problem's characteristics. This adaptive weight adjustment during the evolutionary process improves the algorithm's performance and convergence speed.

2.4.2. Constraints

(1) Coefficient of overturning

In the analysis of train overturning stability, the coefficient of overturning is a critical engineering parameter. It measures the train's ability to remain stable when subjected to external moments, such as side winds or changes in curve radius, during travel. A smaller overturning coefficient indicates a lower likelihood of train overturning and better stability. The calculation formula for the overturning coefficient is as follows:

$$G_3(P) = \eta = \frac{\sum Q_{iA} - Q_{iB}}{\sum Q_{iA} + Q_{iB}} \leq 0.8 \quad (26)$$

In the formula, Q_{iA} and Q_{iB} sum the wheel-rail normal forces for the high and low rails, respectively.

(2) Derailment Coefficient

$$\frac{Y}{Q} = \frac{\tan\alpha - \mu}{1 + \mu\tan\alpha} \quad (27)$$

The ratio between the lateral and vertical forces *(Y/Q)* is often used to indicate the track's mass and reflects the vehicle's safety based on its dynamic behavior. In the Nadel formula, a represents the wheel flange angle, μ is the friction factor between the wheel and rail, and Y and Q represent the lateral and vertical forces, respectively. The Nadel formula illustrates the relationship between the lateral and vertical forces that can be transmitted to the rail without causing derailment.

(3) Geometric Constraints of Curve Tread

The optimized design uses the CN60 and measured profiles with maximum wear as boundary constraints. The constraint function is defined as follows:

$$f_d(y_i) \leq y_i \leq f_u(y_i) \quad i \in (1,2,\cdots,8) \quad (28)$$

$f_d(y_i)$ represents the maximum wear profile, and $f_u(y_i)$ represents the CN60 rail profile. Considering the contact characteristics between the wheel and rail, the wheel-rail contact region, which is also the optimization region, should be defined as a convex curve. Since the rail profile exhibits the characteristics of a convex curve, the slopes between two adjacent points are expected to increase monotonically and continuously. Therefore, these slopes should be constrained according to the position of each control point to ensure the

generation of effective profiles during the optimization process. This constraint reduces the computational time and ensures the production of desirable profiles. The constraint function can be expressed as follows:

$$\begin{gathered}\left(\frac{z_j-z_{j-1}}{y_j-y_{j-1}}\right)\Big/\left(\frac{z_{j+1}-z_j}{y_{j+1}-y_j}\right) \leq 1(j=2,2,\cdots,N_{mov}-1) \\ (z_1-z_a)/(y_1-z_a) \geq S_a \\ \left(z_b-z_{N_{\mathrm{mov}}}\right)/\left(y_b-y_{N_{\mathrm{mov}}}\right) \leq S_b\end{gathered} \quad (29)$$

S_a and S_b represent the slopes of the fixed points at both ends of the optimization region.

2.5. Dynamics Simulation Model

2.5.1. Vehicle Dynamics model

In the dynamics software SIMPACK, a dynamics model of a Chinese A-type subway train is constructed. The vehicle consists of 4 wheelsets, eight axle boxes, two frames, and one body. The axleboxes have only one rotational degree of freedom, while the other rigid bodies have 6 degrees of freedom, resulting in 50 degrees of freedom in the model. Table 2 shows some parameters of the vehicle system. The line parameters include a curve radius of 800 m, a front and rear straight section length of 100 m each, a gentle curve section length of 65 m, a track height of 0.03 m, a curve section length of 280 m, and a total line length of 610 m. The measured track unevenness NC50 is imposed on the entire section throughout the simulation. The LM wheel profile is used.

Table 2. Parameters of Type A Subway Trains.

Vehicle model number	AW3
Vehicle Body Mass/kg	50650
Chassis Mass/kg	2800
Wheelset Mass/kg	1140
Vehicle Fixed Distance/m	15.7
Wheelbase/m	2.5
Rolling Diameter of Wheels/m	0.84
Longitudinal Stiffness of One Series of Steel Springs/ (MN/m)	1.4
Lateral Stiffness of One Series of Steel Springs/ (MN/m)	1.4
Vertical Stiffness of One Series of Steel Springs/ (MN/m)	1.1
Longitudinal Stiffness of Axle Box Pivot Node/ (MN/m)	12
Lateral Stiffness of Axle Box Pivot Node/ (MN/m)	2.5
Longitudinal Stiffness of Air Spring/ (MN/m)	0.12
Lateral Stiffness of Air Spring/ (MN/m)	0.12
Vertical Stiffness of Air Spring/ (MN/m)	0.25

2.5.2. Model Validation

To ensure the accuracy of the multi-body dynamics model of the train, we collected lateral acceleration data of the Type A subway train's car body in the test section. Virtual simulations of the dynamics model were conducted using SIMPACK software, considering the actual working conditions. In the numerical simulation, we used the actual measured rail wear data and a NURBS curve fitting function formula as inputs to obtain the numerical results of the car body's transverse acceleration. These results were then compared and analyzed against the test results.

As shown in Fig.7, the test results indicate that the lateral acceleration of the car body is slightly higher than the simulation results. However, the two are generally consistent. This can be attributed to the fact that the uneven power spectrum used in the simulation is based on the measured NC50 uneven spectrum, which closely resembles the actual track unevenness. Consequently, the test data and model data exhibit a closer match. It should be noted that the dynamic model does not consider the flexible deformation of key rail components such as rails, fasteners, and sleepers. Therefore, there is still some disparity between the simulation and measured data. Nonetheless, the model's calculations closely align with the line test results, indicating that the dynamic model accurately simulates the vehicle's dynamic performance.

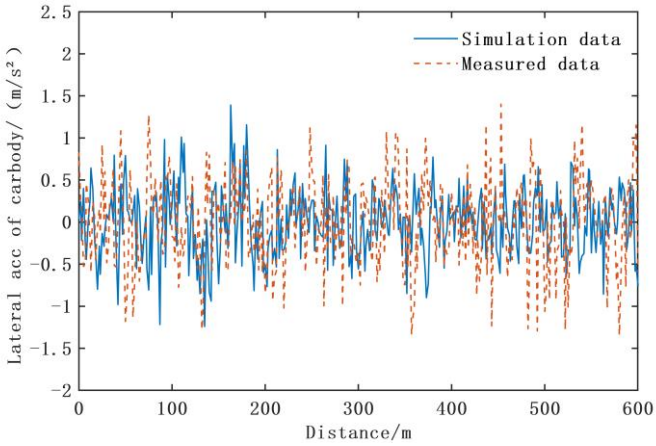

Fig. 7. Comparison between simulated and measured lateral acceleration of the car body

2.5.3. Proxy Model

To simulate the dynamic performance of tens of thousands of wheel profiles and obtain optimal designs, traditional vehicle dynamics simulation software is often time-consuming and resource-intensive, making large-scale simulations impractical. In order to address this issue, a proxy model is employed to approximate the simulation results, reducing computational costs and improving design space search efficiency. This study chooses Radial Basis Functions (RBFs) as the approximate mathematical model among various proxy models. RBFs can accurately model arbitrary functions and excel in handling complex design spaces, multivariate relationships, and nonlinearities27. RBF is relatively straightforward to implement compared to other models such as Kriging, neural networks, and multivariate adaptive regression spline. Therefore, this paper uses the RBF proxy model to establish the mapping relationship between design variables and the objective function for wheel profile optimization design.

To ensure the proxy model's computational accuracy, the Latin hypercubic sampling method is employed for the experimental design of the optimization variables and parametric analysis of the experimental results. This method allows efficient optimization of wheel profiles, and approximate results can be obtained within a shorter timeframe.

Initially, the initial parameters are defined, and the interval values of the objective function and its variables are determined. A sampling design is then performed with 100 samples for the optimization variables, and initial design samples are generated based on these variables. Subsequently, the objective function and constraint values are obtained using the established MATLAB/SIMPACK joint simulation model. Finally, an RBF agent model is created, and its accuracy is evaluated using three metrics:

(1) R^2 (R-squared): R^2 is a measurement used to evaluate the goodness of fit of a proxy model to observed data. It quantifies the proportion of variance in the target variable that the model explains.

(2) RAAE (Relative Average Absolute Error): RAAE is utilized to assess the proxy model's average prediction error. It represents the ratio of the average absolute error between the model's predicted values and the actual observed values relative to the average of the actual observed values.

(3) RMAE (Relative Maximum Absolute Error): RMAE is employed to measure the maximum prediction error of the proxy model. It represents the ratio of the maximum absolute error between the model's predicted value and the actual observed value relative to the average value of the actual observed values.

These evaluation metrics are valuable in determining the accuracy and reliability of the proxy model, allowing for an assessment of its suitability in practical applications as an alternative to more time-consuming simulations. Table 3 presents the results of the three evaluation indexes, demonstrating the high accuracy of the proxy model and its effectiveness in optimizing wheel profiles.

Table 3. Accuracy evaluation criteria for RBF surrogate models.

Objective and constraint functions	R2	RAAE	RMAE
Cumulative wear amount	0.980	0.138	0.316
Grinding removal	0.994	0.116	0.289
Wheelset Lateral force	0.974	0.136	0.344
Derailment coefficient	0.984	0.127	0.320
Coefficient of	0.972	0.135	0.342

2.6. TS-NSGA-II optimization algorithm

NSGA-II is known for its excellent global search capabilities but is weak in local search and susceptible to falling into local optima28. Taboo Search (TS), a widely used meta-heuristic algorithm, is employed to overcome this limitation. TS can explore unexplored regions of the search space and prevent repetitive visits to the same solutions by utilizing a taboo table memory structure. By iteratively moving from the current solution to a more optimal one, TS-NSGA-II enhances the localized search capabilities of NSGA-II, resulting in improved performance and convergence characteristics. The algorithm flow of TS-NSGA-II is depicted in Figure 8.

Similar to NSGA-II, TS-NSGA-II utilizes fast, non-dominated ordering to classify individuals in the population into different frontier classes and measures the densities among individuals using crowding distances to ensure solution diversity. However, TS-NSGA-II deviates from the traditional approach by selecting the first and second-best individuals as parent individuals for crossover and generating two offspring. After sorting the selected samples, the TS program is employed to find better individuals, resulting in D1 and D2. Finally, the

two best individuals from S1, S2, C1, C2, D1, and D2 are selected, and this process is repeated until a new population is generated. The TS algorithm requires parameter tuning, including setting stopping conditions, taboo table length, maximum number of iterations, etc. The parameter settings used in this study are presented in Table 4.

Table 4. Parameter settings for TS-NSGA-II.

Population size	Iterations (NSGA-II)	Crossover rate	Mutation rate	Iterations (TS)	Tabu list length
100	100	0.9	0.1	20	50

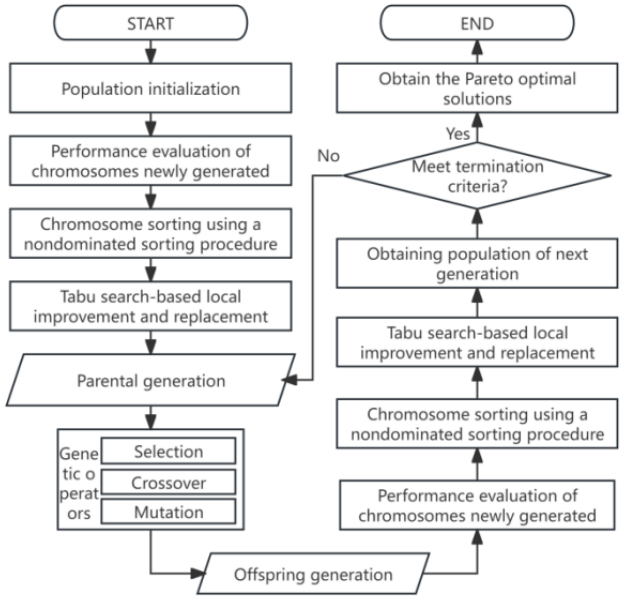

Fig.8. Population iteration and update process of the TS-NSGA-II algorithm.

2.7. Optimization Results

The TS-NSGA-II algorithm is employed to optimize the design variables and achieve the desired objectives and constraints, using the RBF agent model to establish the mapping relationship. The NSGA-II algorithm is then utilized to obtain 100 Pareto optimal solutions within a specific number of iterations. The optimization was conducted on a high-performance workstation with an Intel Core i9 processor, 64GB RAM, and NVIDIA GeForce RTX 3090 graphics card. Each iteration, which involves stochastic operations such as crossover and mutation in the genetic algorithm, takes approximately 20 to 30 minutes to compute. The optimization process, including parameter setting, model training, optimization computation, and result analysis, takes around 2 to 3 days to complete, based on several calibration calculations. The responses of the three objective functions can be observed in Figure 9.

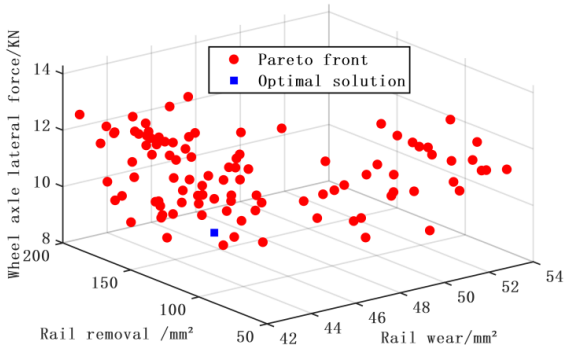

Fig. 9. Optimization results obtained from the TS-NSGA-II algorithm

The red dots represent the Pareto frontiers obtained at the end of the iteration, and the weight adjustment coefficients are determined based on the solution set. After careful consideration, the 94th sample from the 100th iteration is selected as the final optimized solution (represented by blue dots). The results of the iterative calculations are presented in Table 5.

Table 5. Numerical changes of the objective function and constraint function during the iteration process

Number of iterations	Cumulative Wear/mm²	Grinding removal/ mm²	Wheelset lateral force /KN	Fitness	Constraint
20	241.38	29.51	20.68	0.97	Satisfied
40	226.55	27.71	19.67	0.86	Satisfied
60	213.41	26.55	18.54	0.79	Satisfied
80	188.56	21.47	16.24	0.63	Satisfied
100	183.76	21.13	15.94	0.60	Satisfied

2.7.1. Analysis of Rail Grinding Removal and Wear Evolution

Fig.10 illustrates the profiles before and after optimization and compares the amount of rail grinding removal before and after optimization. In order to compare the amount of rail grinding removal before and after optimization, the profiles are shifted downward to the point where there is only one tangent to the rail head curve, aligning them with the wear-representative profile. Based on Fig.10, when the CN60 profile is taken as the grinding target profile, the drop height of the high rail top is 2.74

mm, resulting in an area of rail material removal of 161.22 mm2. Similarly, the drop height of the low rail top is 1.72 mm, with an area of rail material removal of 102.81 mm2. However, when the optimized profile is used as the grinding target profile, the drop height of the high rail top is reduced to 1.62 mm, which is 1.12 mm less than before optimization.

Additionally, the area of rail material removal decreases to 109.45 mm2, representing a reduction of 32.11%. Similarly, the drop height of the low rail top is reduced to 0.98 mm, which is 0.65 mm less than before optimization. The area of rail material removal is reduced to 74.31 mm2, representing a reduction of 27.72%.

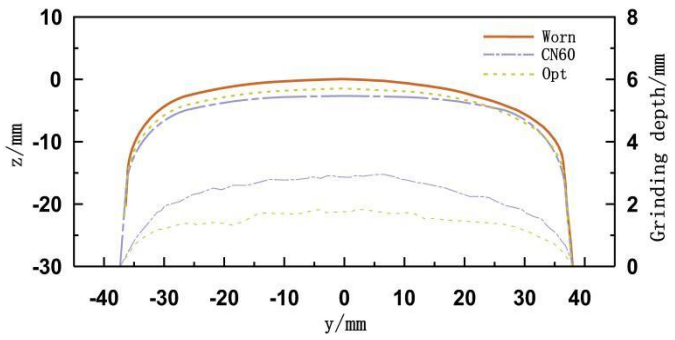

(a） High rail

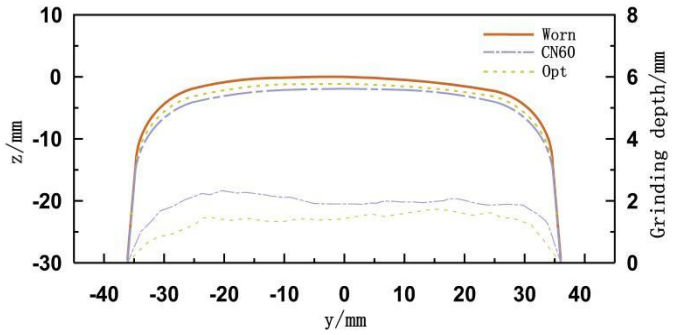

(b） Low rail

Fig.10. Comparison of rail grinding profile.

Fig.11 compares rail wear on the circular curve profile before and after optimization at different total numbers of passes. When the total number of passes reaches 9×106, the maximum wear depth of the high rail prior to optimization is 0.584 mm, while the maximum wear depth of the low rail is 0.382 mm. After optimization, the wear depth of the high rail is reduced to 0.392 mm, representing a reduction of 32.9%. Similarly, the maximum wear depth of the low rail is reduced to 0.278 mm, representing a reduction of 27.2%.In terms of predicted wear, the area of wear for the high rail is reduced from 16.25 mm2 to 10.61 mm2, indicating a reduction of 34.7%. For the low rail, the wear area is reduced from 9.85 mm2 to 7.24 mm2, representing a reduction of 26.4%.

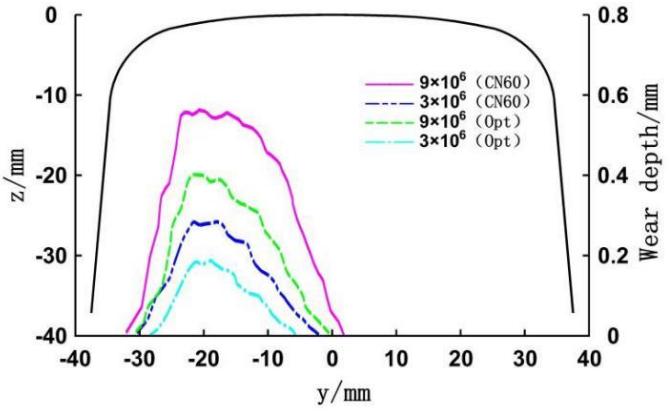

(a)High Rail

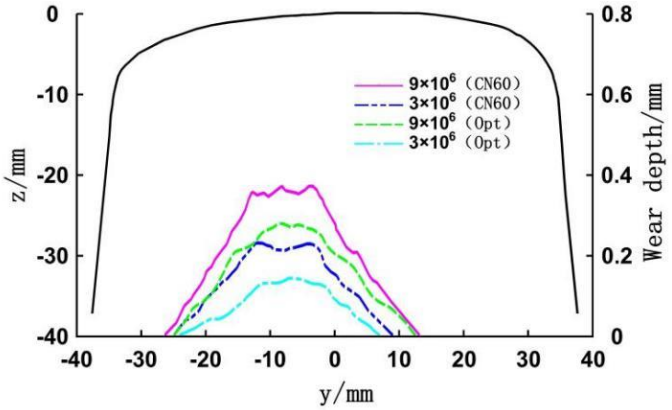

(b)Low Rail

Fig.11. Accumulated Wear under Different Throughput Levels.

2.7.2. Wheel-Rail Static Contact Geometry Analysis

Both the CN60 and Opt profiles are employed in the analysis of wheel-rail contact static geometry. The bottom rail slope is set at 1/40, and the gauge is fixed at 1435 mm. Fig.12 illustrates the wheel-rail contact states of the CN60 and Opt profiles matched with the LM rail profile.

From the Fig, it can be observed that prior to optimization, the lateral displacement falls within the range of [-4 mm, -8 mm]. This indicates the wheel-rail contact point jumping from the rail top region to the rail gauge angle contact region. The contact points on the low rail are primarily concentrated at the top, with additional jumps occurring in the rail gauge angle transition region within the range of lateral displacement [6 mm, 10 mm]. These conditions result in concentrated wheel-rail contact points on the rail, leading to uneven wear of the rail and a reduction in the wheel-rail service life.

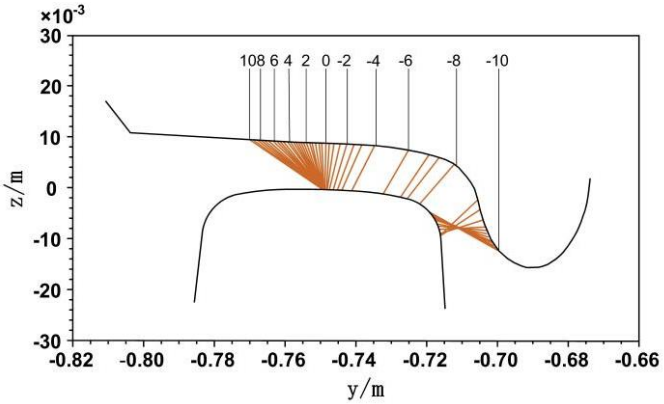

(a)High rail(CN60)

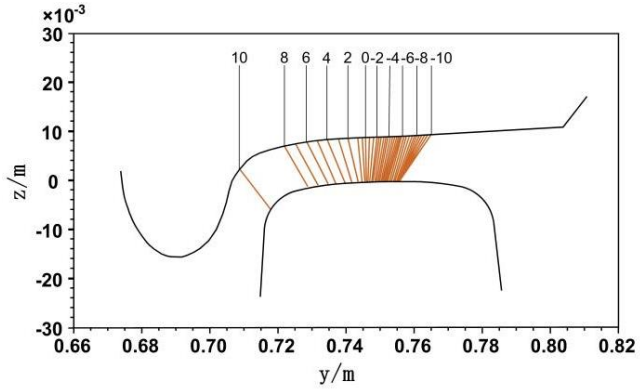

(b)Low rail(CN60)

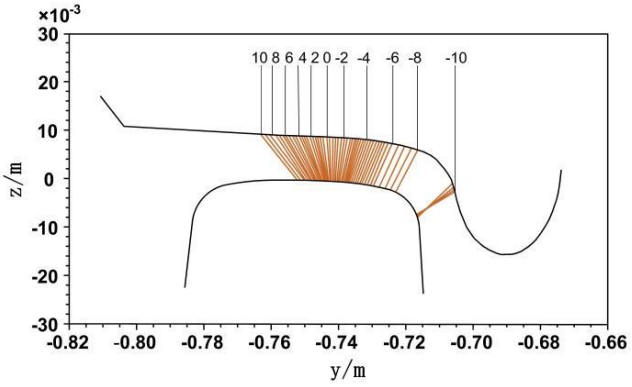

(c)High rail(Opt)

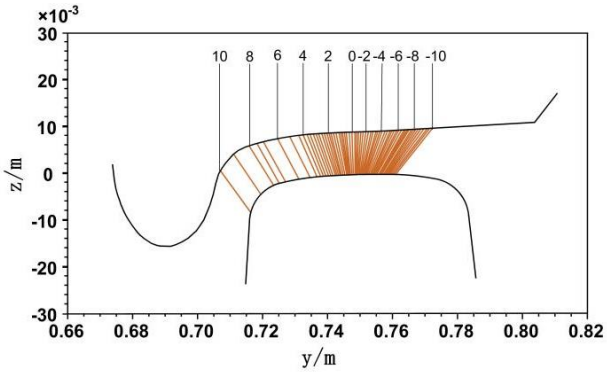

(d)Low rail(Opt)

Fig.12. Distribution map of wheel-rail contact spots before and after optimization.

After optimization, the contact points of the high rail are primarily located at the top of the rail, with no significant jump points observed. Furthermore, the zero-transverse contact point of the high rail is shifted inward by approximately 6.9mm, while the zero-transverse contact point of the low rail is shifted outward by about 6.1mm compared to the CN60 profile. This shift results in a larger wheel-rail track diameter difference, enhancing the train's performance when traversing curves. Additionally, compared to the CN60 profile, the contact point of the high rail's rail head is biased more towards the outer side of the rail, closer to the center of the rail head. The wheel-rail contact point of the low rail at the outer side of the top of the rail is more uniformly distributed, resulting in a wider distribution of the rail head's contact point. This helps to reduce contact stress on the rail and mitigate local rail wear.

The rolling circle radius difference is a crucial parameter that reflects a vehicle's ability to navigate curves and its serpentine instability. By analyzing the matching status of the rail profile and LM wheel profile before and after optimization, the correlation between the rolling circle radius difference of the wheelset and the wheelset traverse can be determined. As depicted in Fig.13, in the range of [9.5,10mm], the wheelset's rolling circle radius difference remains similar for both rail profiles. However, in the range of [0,9.5mm], the rolling circle radius difference of the optimized profile is larger than that of the CN60 profile. This larger rolling circle radius of the wheelset helps reduce the transverse displacement of the vehicle when traversing curves, thereby improving vehicle stability, safety, and curve-passing performance.

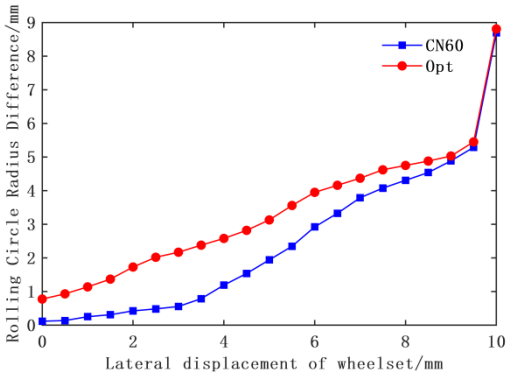

Fig.13. Comparison of RRD

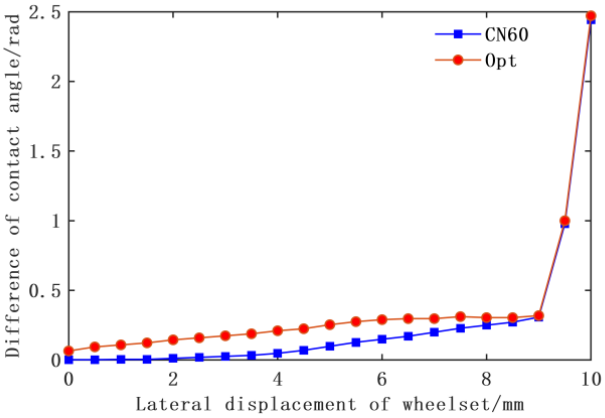

Fig.14. Difference of wheel/rail contact angle.

The wheel-rail contact angle difference curve significantly impacts the wheel-rail contact stiffness. It influences the relationship between the wheel-pair rolling circle radius difference and the wheel-pair traverse. This relationship is crucial for the vehicle's curve-passing performance. Fig.14 illustrates the contact angle difference curve of the LM wheel profile matched with the rail before and after optimization.

From the Fig, it can be observed that the contact angle difference of the optimized profile is larger than that of the CN60 profile within the wheel pair traverse range of [0 mm, 9.5 mm]. Increasing the contact angle difference has several benefits. It helps enhance the rail's transverse guiding force in the curved section, reducing wear and deformation of the rail gauge angle. Moreover, it improves the train's lateral stability, ultimately improving overall performance during curve traversal.

2.7.3. Analysis of Curve Passing Performance

In this analysis, we focused on the CN60 profile and the train's first wheelset, with the optimized profile matched to the LM wheel profile. Various performance indicators were calculated, including the train body's lateral acceleration, wheel-rail transverse force, derailment coefficient, wheel-weight reduction rate, and change in wheelset transverse displacement. The mean values of the data from the circular curve section were used for the analysis.

The lateral acceleration of the train body is a key indicator for evaluating vehicle sway and comfort. A low-pass filtering process with a cutoff frequency of 10 Hz was applied to the lateral acceleration data of the train body. As shown in the graph in Fig.15, both the original bogie configuration and the optimized rail profile showed no instability. However, the results indicate that the optimized rail profile improved the lateral stability of the train body. This demonstrates that rail optimization can enhance the lateral stability of the train body, effectively reducing vehicle oscillations and improving ride comfort.

Fig.16 illustrates the comparison of wheel-rail transverse forces before and after optimization. Prior to optimization, the mean value of the high rail transverse force was -7.27 kN, while the mean value of the low rail transverse force was 5.17 kN. After optimization, these values were reduced to -5.32 kN and 4.26 kN, respectively, representing reductions of 26.9% and 17.6%. By reducing the lateral forces, the risk of side slip and derailment in the curve section can be effectively mitigated, resulting in a lower derailment coefficient. This risk reduction not only decreases maintenance costs but also enhances the safety of train operations.

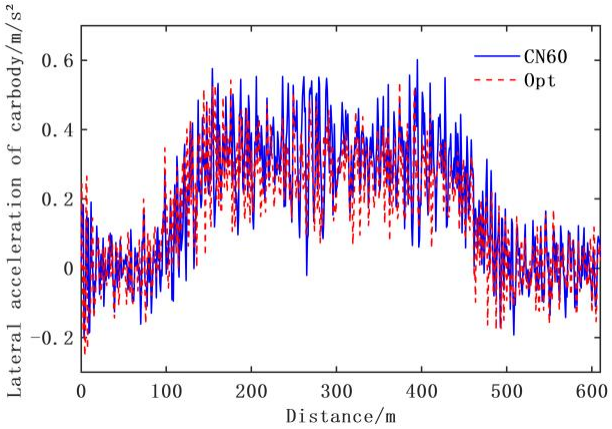

Fig.15. Lateral acceleration of car body

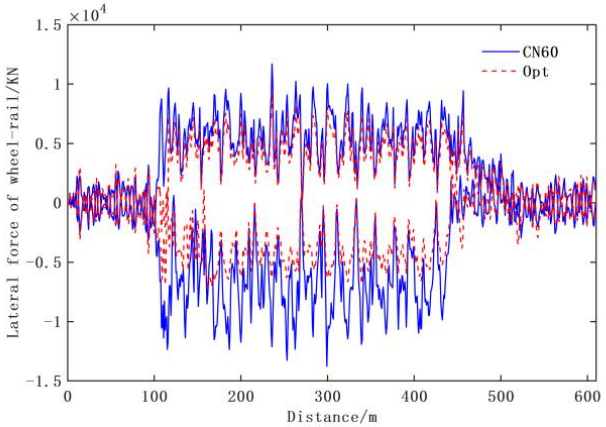

Fig.16. Lateral forces of wheel/rail

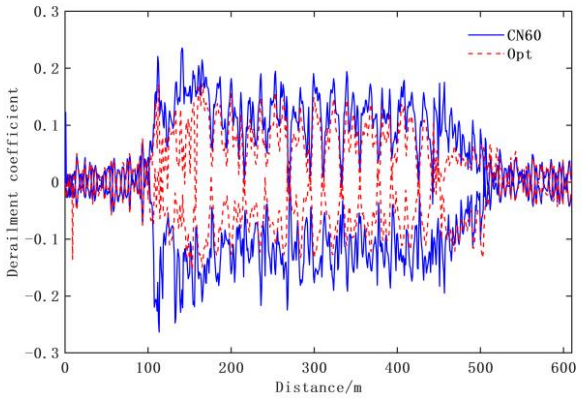

Fig.17. Derailment coefficient.

In order to assess the overturning performance of the speed-enhanced freight train before and after rail grinding, the wheel load reduction rate is shown in Fig.18. It can be observed that rail grinding equalizes the left and right wheel weights of the train wheelset on the curve by increasing the difference in wheel diameters, resulting in a reduction of approximately 24.5% in the wheel load reduction rate.

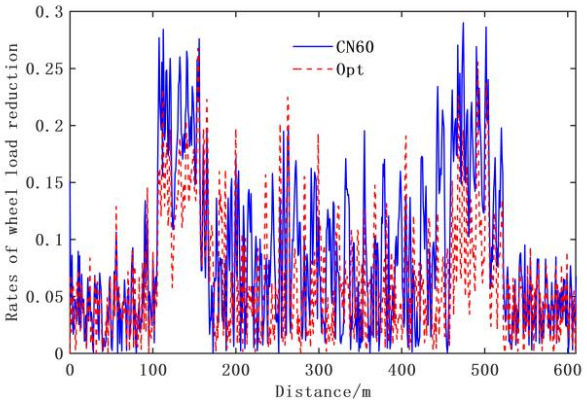

Fig.18. Rates of wheel load reduction

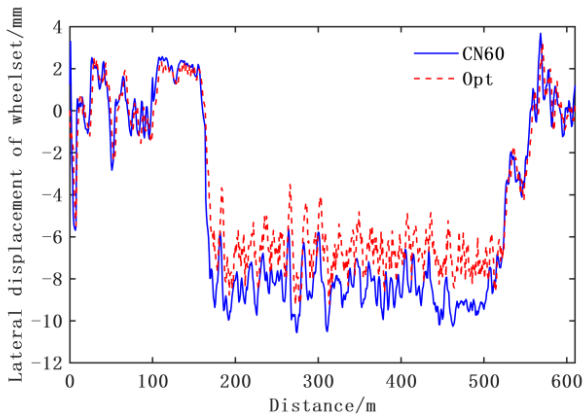

Fig.19. Lateral displacement of wheelsets.

The optimized profile improves the balance of the wheelsets' left and right wheel weights through the increase in rolling circle radius. Compared to the CN60 profile, the optimized profile significantly reduces the average lateral displacement of the wheelsets from 8.67 mm to 7.24 mm before grinding, representing a reduction of 16.5%. The comparison of Figs 15-19 demonstrates the improved kinetic performance of the optimized rail profiles. Moreover, the kinetic performance indices of the optimized profiles fall within the superior class of rolling stock kinetic performance29.

3. Conclusion

（1）This study utilized the dynamic time regularization algorithm (DTW) to select representative worn profiles that accurately reflect rail wear as the initial population for optimization. This approach reduces the search space and increases the convergence speed and reliability of the optimization results.

（2）In this study, a multi-objective rail profile optimization model considering wear evolution has been developed, and the wear simulation capability has been successfully integrated into the dynamics simulation module. This model enables accurate prediction of wheel profile wear. To achieve the optimal design of the rail grinding profile, the TS-NSGA-II algorithm is employed to solve this wheel profile optimization model. This optimization algorithm can be used to obtain the optimal design of the rail grinding profile.

（3）The static wheel-rail contact relationship between different LMa wheel profiles was analyzed. The optimized profiles exhibited a more uniform distribution of contact points, which helps slow down local rail wear. The rolling circle radius difference and wheel-rail contact angle difference were improved, enhancing the curve passing performance of the vehicle in curved sections. Furthermore, various performance indicators were significantly improved, including vehicle lateral acceleration, maximum lateral forces on the wheels and rail, derailment coefficient, wheel weight reduction rate, and transverse displacement.

（4）A comparison of the profile before and after optimization as a rail grinding profile shows that after optimization, the grinding drop height of the top of the outer rail is reduced by 1.12mm, the grinding drop height of the top of the inner rail is reduced by 0.65mm, and the total rail material removal area is

reduced by 30.4%, which effectively reduces the amount of rail grinding removal.

（5） Considering the need for simplified data requirements, experimental validation, computational efficiency, and accuracy, the equivalent elastic contact method was utilized to predict wheel-rail wear. However, this method may have limitations in accurately capturing the complexity of the wheel-rail contact region. Therefore, future studies will investigate the feasibility of incorporating a discrete elastic contact model to enhance the prediction's accuracy and comprehensiveness.

Reference

1. Lin Q, Guo J, Wang H, Wang W，Liu Q. Optimal design of rail grinding patterns based on a rail grinding target profile. Proc Inst Mech Eng Part F J Rail Rapid Transi 2018; 232(2): 560-571, https://doi.org/10.1177/0954409716679447.
2. Li D, Wei K, Chen R, Xu Y. Analysis of Heavy Hual Railway Wear on Wheel/Rail Contact. Geometry ICTE 2015; 64-69, https://doi.org/10.1061/9780784479384.009.
3. Wang P, Gao L, Xin T, Cai X, Xiao H. Study on the numerical optimization of rail profiles for heavy haul railways. Proc Inst Mech Eng Part F J Rail Rapid Transit 2017; 231(6): 649-665, https://doi.org/10.1177/0954409716635685.
4. Zeng, W, Yang Y, Qiu W, Xie H, Xie S. Optimization of the target profile for asymmetrical rail grinding in sharp-radius curves for high-speed railways. Adv Mech Eng 2017; 9: 1687814016687196, https://doi.org/10.1177/1687814016687196.
5. Liang X, Zheng M. Estimation of rail vertical profile using an h-infinity based optimization with learning. ASME/IEEE Joint Rail Conference. American Society of Mechanical Engineers, 2019; 58523: V001T01A007, https://doi.org/10.1115/JRC2019-1266.
6. Huang K，Wu J, Yang X, Gao Z, Liu F, Zhu Y. Discrete Train Speed Profile Optimization for Urban Rail Transit: A Data-Driven Model and Integrated Algorithms Based on Machine Learning. Journal of Advanced Transportation 2019; 2019, https://doi.org/10.1155/2019/7258986.
7. Ye Y, Qi Y, Shi D, Sun Y, Zhou Y, Hecht M. Rotary-scaling Fine-tuning (RSFT) Method for Optimizing Railway Wheel Profiles and Its Application to A Locomotive. Railway Engineering Science 2020; 28: 160-183, https://doi.org/10.1007/s40534-020-00212-z.
8. Jiang H, Gao L. Optimizing The Rail Profile for High-Speed Railways Based on Artificial Neural Network and Genetic Algorithm Coupled Method. Sustainability 2020; 12(2): 658, https://doi.org/10.3390/su12020658.
9. de Paula Pacheco PA, Endlich CS, Vieira KLS, Reis T, dos Santos GFM, dos Santos Júnior AA. Optimization of Heavy Haul Railway Wheel Profile Based on Rolling Contact Fatigue and Wear Performance. Wear 2023; 522: 204704, https://doi.org/10.1016/j.wear.2023.204704.
10. Qi Y, Dai H, Gan F, Sang H. Optimization of Rail Profile Design for High-speed Lines Based on Gaussian Function Correction Method. Proc Inst Mech Eng Part F J Rail Rapid Transit 2023; 237(9): 1119-1129, https://doi.org/10.1177/09544097231152564.
11. Lin F, Zou L, Yang Y, Shi Z. Design method of worn rail grinding profile based on Frechet distance method. Proc Inst Mech Eng Part F J Rail Rapid Transit 2022; 236(8): 936-949, https://doi.org/10.1177/09544097211049650.
12. Shi J, Gao Y, Long X, Wang Y. Optimizing rail profiles to improve metro vehicle-rail dynamic performance considering worn wheel profiles and curved tracks. Structural and Multidisciplinary Optimization 2021; 63: 419-438. https://doi.org/10.1007/s00158-020-02680-7.
13. Zhai W, Gao J, Liu P, Wang K. Reducing rail side wear on heavyhaul railway curves based on wheel–rail dynamic interaction. Veh Sys Dyn 2014; 52(sup1): 440-454, https://doi.org/10.1080/00423114.2014.906633.
14. Mao X, Shen G. An inverse design method for rail grinding profiles. Veh Sys Dyn 2017; 55(7): 1029-1044, https://doi.org/10.1080/00423114.2014.906633.
15. Wang J, Chen S, Li X, Wu Y. Optimal rail profile design for a curved segment of a heavy haul railway using a response surface approach. Proc Inst Mech Eng Part F J Rail Rapid Transit 2016; 230(6): 1496-1508, https://doi.org/10.1177/0954409715602513.
16. Choi H, Lee D, Song C, Lee J. Optimization of rail profile to reduce wear on curved track. International Journal of Precision Engineering and Manufacturing 2013; 14: 619-625, https://doi.org/10.1007/s12541-013-0083-1.
17. Xu K, Feng Z, Wu H, Xu D, Li F, Shao C. Optimal profile design for rail grinding based on wheel–rail contact, stability, and wear development in high-speed electric multiple units. Proc Inst Mech Eng Part F J Rail Rapid Transit 2020; 234(6): 666-677, https://doi.org/10.1177/0954409719854576.

18. Liu B, Mei T, Bruni S. Design and optimization of wheel–rail profiles for adhesion improvement. Veh Sys Dyn 2016; 54(3): 429-444, https://doi.org/10.1080/00423114.2015.1137958.
19. Qi Y, Dai H, Wu P, Gan F, Ye Y. RSFT-RBF-PSO: a railway wheel profile optimization procedure and its application to a metro vehicle. Veh Sys Dyn 2021; 60(10): 3398-3418, https://doi.org/10.1080/00423114.2021.1955135.
20. Ding J, Lewis R, Beagles A, Wang J. Application of grinding to reduce rail side wear in straight track. Wear 2018; 402: 71-79, https://doi.org/10.1016/j.wear.2018.02.001.
21. Ren D, Tao G, Wen Z, Jin X. Wheel profile optimization for mitigating flange wear on metro wheels and verification through wear prediction. Veh Syst Dyn 2020; 59(12): 1894-1915, https://doi.org/10.1080/00423114.2020.1798472.
22. Ye Y, Vuitton J, Sun Y, Hecht M. Railway wheel profile Fine-Tuning system for profile recommendation. Railway Engineering Science 2021; 29: 74-93, https://doi.org/10.1007/s40534-021-00234-1.
23. Lin F, Zhou S, Dong X, Xiao Q, Zhang H, Hu W. Design method of LM thin flange wheel profile based on NURBS. Veh Syst Dyn 2021; 59(1): 17-32, https://doi.org/10.1080/00423114.2019.1657908.
24. Han T, Peng Q, Zhu Z, Shen Y, Huang H, Abid N. A pattern representation of stock time series based on DTW. Physica A: Statistical Mechanics and its Applications 2020; 550: 124161, https://doi.org/10.1016/j.physa.2020.124161.
25. Braghin F, Lewis R, Dwyer-Joyce R, Bruni S. A mathematical model to predict railway wheel profile evolution due to wear. Wear 2006; 261(11-12): 1253-1264, https://doi.org/10.1016/j.wear.2006.03.025.
26. Li J, Tao G, Liu X, Liang H, Wen Z. Comparative analysis of metro wheel wear prediction based on two trackmodeling methods. Engineering Mechanics 2022; 39(6): 226-235, https://doi.org/10.6052/j.issn.1000-4750.2021.02.0117.
27. Dong J, Li Y, Wang M. Fast multi-objective antenna optimization based on RBF neural network surrogate model optimized by improved PSO algorithm. Applied Sciences 2019; 9(13): 2589, https://doi.org/10.3390/app9132589.
28. VERMA S, PANT M, SNASEL V. A comprehensive review on NSGA-II for multi-objective combinatorial optimization problems. IEEE access 2021; 9: 57757-57791, https://doi.org/10.1109/ACCESS.2021.3070634.
29. GB5599-2019. Specification for dynamic performance evaluation and test appraisal of railway vehicles. Ministry of Railways of the People's Republic of China, 2019.